ULRR

Dual parametric sensors based on multi-core fiber

Item Type	Meetings and Proceedings
Authors	Yu, Liu;Yang, Chan;Yang, Jing;Shi, Jinhui;Guan, Chunying
Citation	20th Sensors and Their Applications Conference, 2024, Paper No: 29
Publisher	University of Limerick
Download date	2026-02-18 00:19:57
Item License	https://creativecommons.org/licenses/by-nc-sa/4.0/
Link to Item	https://doi.org/10.34961/researchrepository-ul.29279153

29: DUAL PARAMETRIC SENSORS BASED ON MULTI-CORE FIBER

Liu Yu, Chan Yang, Jing Yang, Jinhui Shi, Chunying Guan**

College of Physics and Optoelectronic Engineering, Harbin Engineering University, Harbin 150001, China

Optical Fibre Sensors 1, EM010, August 12, 2024, 1:30 PM - 3:00 PM

Abstract – Two optical fiber sensors based on a hole-assisted dual-core fiber (HADCF) and a hole-assisted three-core fiber (HATCF) have been proposed and experimentally demonstrated for dual-parameter measurements respectively. For the sensor based on HADCF, the dual-mode interferometer created uses the LP_{01} mode and LP_{11} mode in the suspended core, combined with a directional coupler formed by using the suspended core and the center core in a 16 mm long HADCF. For the sensor based on HATCF, two directional couplers are formed by using the suspended cores and the center core in an 8 mm long HATCF. The dual parameter measurement can be achieved through monitoring the interference dips and resonance dips. The proposed sensors have outstanding advantages such as simple structure, high integration and dual parameter measurement, making them potentially applications in the field of biological detection.

***Keywords*:** dual parameter measurement; multi-core fiber; directional coupler

1. INTRODUCTION

Refractive index (RI) is a fundamental parameter reflecting the properties of liquids and can play an important role in the fields of biomedicine, environmental protection, and food safety [1], etc. The optical fiber RI sensors based on different structures and principles have been proposed, such as photonic crystal fibers (PCFs) [2], surface plasmon resonance (SPR) [3], interferometers [4], gratings [5-6] and couplers [7]. In 2016, a RI sensor based on Mach-Zehnder interferometer (MZI) was proposed [4]. Two tapers cascaded in a single mode fiber (SMF) generate the interference between core mode and cladding mode, and the RI sensitivity reaches 158.4 nm/RIU. This sensor is easy to fabricate, but the sensitivity is low and the tapering process will affect the mechanical strength of the sensor. An MZI RI sensor with the sensitivity of 260.8 nm/RIU based on PCF was proposed [2]. However, the high cost of PCF limits the application of such sensors. In 2017, an in-fiber RI sensor based on single eccentric hole-assisted dual-core fiber was proposed [7]. By filling different RI liquid into the air hole, the RI sensitivity of the resonance wavelength between the suspended core and the center core reaches 627.5 nm/RIU. This RI sensor has advantages of good mechanical strength and high sensitivity, however, the RI of the liquid is inevitably affected by temperature, which will lead to the temperature crosstalk.

To suppress temperature crosstalk, many dual-parameter sensors for RI and temperature measurement were proposed. Liu et al. demonstrated a miniature all-fiber sensor based on composite structure of Fabry-Perot interferometer (FPI) and fiber Bragg grating (FBG), the temperature and RI sensitivities of the FPI are -0.189 nm/°C and 1210.490 nm/RIU, respectively [5]. FBG is not sensitive to RI and its temperature sensitivity is 0.011 nm/°C. Chen et al. proposed an all-fiber sensor based on a microprobe with an ultra-short phase-shifted FBG and a common FBG to achieve dual-parameter measurement [6], but the two sensing elements based on different principles will complicate the preparation process and increase the size of the sensor.

In this work, we experimentally demonstrated two all-fiber sensors based on a hole-assisted dual-core fiber (HADCF) and a hole-assisted three-core fiber (HATCF) respectively for simultaneous measurement of RI and temperature. An MZI and a directional coupler fit together well in a single HADCF by splicing a segment of HADCF between two single mode fibers (SMFs) with an offset. Two directional couplers fit together in an 8 mm long HATCF. An air hole is opened by femtosecond laser to expose the suspended core to external environment. The proposed sensor has compact structure, high integration and high sensitivity, making it potentially applications for the field of biological detection.

1. METHODS AND PROCEDURES

The cross-section photographs of HADCF and HATCF are shown in Fig. 1. The HADCF comprises a silica cladding, a center core, a suspended core and a large air hole, where their diameters are 125 μm, 10 μm, 12 μm, and 35 μm, respectively. The air hole is located at the side of the center core. The suspended core used is suspended on the inner wall of the air hole, which is the closest location to the center core. The distance between the centers of the suspended core and the center core was 15 μm and the RI difference between the core and the cladding was 0.005. The HATCF is composed of a center core, two identical suspended cores, two air holes and a cladding. Two suspended cores are attached to the inner side of the air holes closest to the center core. The angle between the center core-suspended core 1 connecting line and the center core-suspended core 2 connecting line is about 110°. The diameters of the center core, suspended cores, air holes and cladding are 8.5, 11.2, 36.9, 125 μm, respectively. The distance between the edges of the suspended core and the center core is 4.8 μm. The RI difference between the center core and cladding is 0.005.

Due to the small distance between the center core and the suspended cores, the fiber can be used as a directional coupler at the phase-matching wavelength. According to the coupling-mode theory, the amplitudes of the optical field in the cores satisfy the following equation:

$$\frac{dA_m(z)}{dz} = -j\sum_{m\neq n} K_{mn} A_n(z) e^{i(\beta_m-\beta_n)z} \tag{1}$$

where A_m, A_n, β_m, β_n are the amplitudes and the propagation constants of the modes in each core respectively. The propagation constant β can be written as kn_{eff}. K_{mn} and K_{nm} are the coupling coefficients between the modes in two different cores.

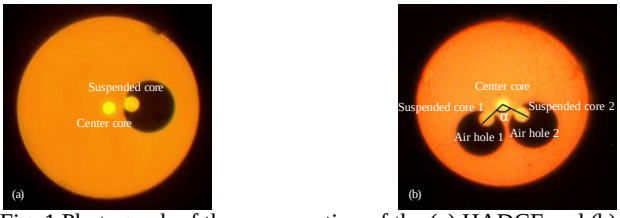

Fig. 1 Photograph of the cross section of the (a) HADCF and (b) HATCF.

According to the Eq. (1), resonance coupling can occur when the propagation constants of guide modes in two cores are equal or extremely close. To determine the resonance wavelength, the effective RIs of the low-order modes in the cores against the wavelength were calculated by using finite element method and are shown in Fig. 2. For the HADCF, as the wavelength increases, the effective RIs of the guide modes decrease. The effective RIs of suspended cores decrease faster due to the different dispersion characteristics between silica and air. The dispersion curves of the fundamental modes of the center core and the suspended core intersect at a wavelength of 1350 nm. The LP_{11} mode in the suspended core cuts off at ~1410 nm. For the HATCF, at 1550 nm, the effective RIs of fundamental modes in two cores are equal, which means resonance coupling can occur here. The LP_{11} mode in the suspended core cuts off at ~1410 nm.

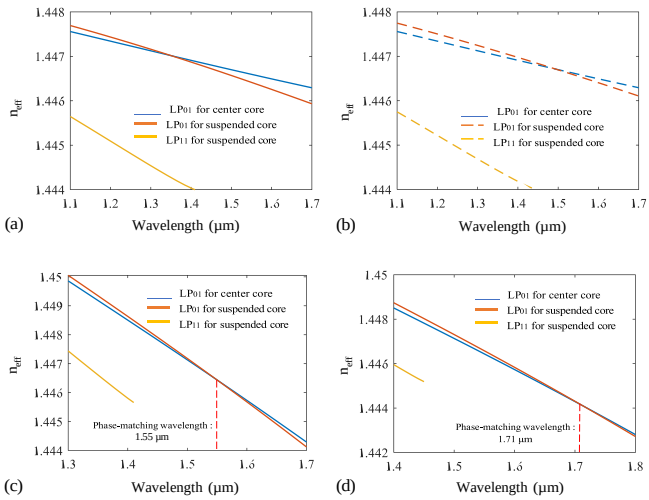

Fig. 2 (a) and (b) The calculated dispersion curves for the low-order modes of the (a) air-filled and (b) water-filled HADCF. (c) and (d) The calculated dispersion curves for the low-order modes of the (c) air-filled and (d) water-filled HATCF.

The structure of the proposed HADCF-based sensor is shown in Fig. 3. The sensor is composed of a section of the HADCF and two SMFs. Both ends of the suspended core are fused to the SMFs with an appropriate offset, as shown in Fig. 3(b). Two micropores near the offset fusing points were fabricated by using femtosecond laser micromachining, to build a microfluidic channel, as shown in Fig. 3(c). The beam from the input SMF passes into the HADCF through the first offset fusing point, allowing the LP_{01} and LP_{11} modes in the suspended core to be excited simultaneously. At the second offset fusing point, the two modes were combined and coupled into the output SMF to form an MZI. The intensity of the interference in the MZI can be expressed as:

$$I = I_1 + I_2 + 2\sqrt{I_1 I_2}\cos(\Delta\varphi) \tag{2}$$

where I_1 and I_2 are the intensities of the light in the LP_{01} and LP_{11} modes in the suspended core. The phase difference between the LP_{01} and LP_{11} modes can be represented by:

$$\varphi = (2\pi\Delta n_{eff} L)/\lambda \tag{3}$$

The free spectra range (FSR) can be expressed as shown below:

$$FSR = \lambda^2/(\Delta n_{eff} \cdot L) \tag{4}$$

where L is the length of the HADCF, and Δn_{eff} is the RI difference between the LP_{01} and LP_{11} modes.

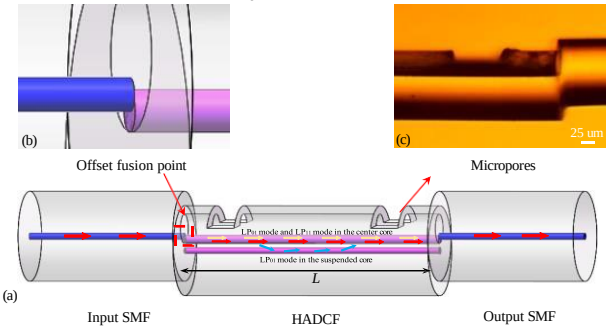

Fig. 3 (a) Schematic configuration of the sensor based on HADCF(b) Enlarged lateral view near the offset point. (c) Micrograph of a micropore fabricated by using a femtosecond laser.

To achieve better interference visibility, the LP_{01} and LP_{11} modes in the suspended core need to be excited equally. With the different offsets, the excitation efficiencies of the LP_{01} and LP_{11} modes in the suspended core are different. At 1210 nm, when the offset was 4.72 μm, the excitation coefficients of the LP_{01} and LP_{11} modes were equal which can obtain the maximum extinction ratio in the interference spectrum.

Meanwhile, due to the small distance between the center core and the suspended core, the HADCF can be regarded as a directional coupler. When the air hole is filled with liquid, the effective RI of the fundamental mode of the suspended core increases as the RI around the core becomes large. Meanwhile, the center core is not affected, so that the phase matching wavelength changes it redshifts. Figure 1(b) shows the calculated effective RIs for different low-order modes in the center and suspended cores of a water-filled HADCF.

The structure of the proposed HATCF-based sensor is shown in Fig. 4. The sensor is constructed by sandwiching a section of the HATCF between two SMFs. Both ends of the center core of the HATCF are spliced to the SMFs without the offset. The beam from input SMF is transmitted directly into the center core of the HATCF. An air hole (marked as hole 1) is opened by femtosecond laser micromachining as a liquid channel. Because of the small distance between the center core and the suspended cores, the HATCF can be seen as two directional couplers. Due to the same RIs and geometric parameters of the two suspended cores, the phase-matching wavelengths between center core and two suspended cores are the same. According to previous analysis, the effective RIs of center core and two suspended cores are equal at 1550 nm. Therefore, strong resonance coupling can

occur here. When the length of the HATCF is an odd multiple of the coupling length, the deepest resonance dip will be obtained.

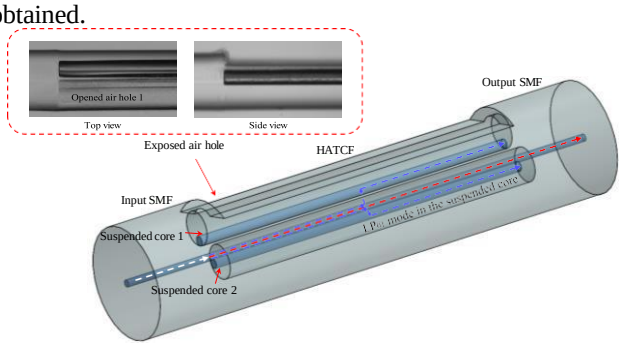

Fig. 4 Schematic configuration of the sensor based on HATCF

Figure 1(d) shows the calculated mode effective RIs of the center and suspended cores in water-filled HATCF. When liquid is filled into the open air hole 1, the RI around the suspended core 1 becomes large, which leads to the increase of mode effective RI in suspended core 1 in the open air hole 1. But the effective RI of the mode in center core is not obviously affected, so that the phase-matching wavelength between center core and the suspended core 1 redshifts to 1710 nm. Meanwhile, the suspended core 2 in the whole air hole 2 is not affected, so that the phase-matching wavelength between the suspended core 2 and the center core is still at 1550 nm. Therefore, the resonance coupling will occur between the center core and the two suspended cores at different wavelength. Hence, two dips will be generated in the transmission spectrum. The resonance dip generated by center core and suspended core 1 in the open hole 1 is sensitive to liquid RI and temperature, while the resonance dip generated by center core and suspended core 2 in the whole hole 2 is only sensitive to temperature. Hence, the simultaneous measurement of temperature and liquid RI can be realized by monitoring the wavelength shifts of the two dips. The demodulation of temperature and RI can be achieved by the coefficient matrix.

2. RESULTS AND DISCUSSION

The sensor based on HADCF was used to detect the characteristics of the salinity and the temperature.

Figures 5(a) and 5(b) show the transmission spectra of the sensor before and after filling with liquid. Their spatial frequency spectra were shown in Figs. 5(c) and 5(d), respectively. Before filling with liquid, the multiple interference dips caused by LP_{01} and LP_{11} modes in the suspended core were observed in the wavelength range of 1100 -1300 nm. In the wavelength range of 1300 - 1400 nm, an obvious resonance coupling dip is seen, overlapping with

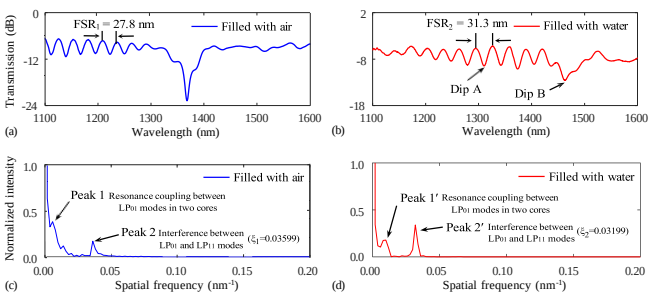

Fig. 5 Transmission spectra and spatial frequency spectra of sample. (a), (c) without liquid and (b), (d) filled with liquid.

the interference spectrum. Interference dips disappear when the LP_{11} mode in the suspended core cuts off beyond a wavelength of ~1410 nm. The Peak 1 in Fig. 5(c) can be attributed to the resonance coupling between LP_{01} modes in the center and suspended core. While the Peak 2 can be attributed to the interference between LP_{01} and LP_{11} modes in the suspended core, as the reciprocal of the spatial frequency (ξ_1) of the Peak 2 is equal to the FSR of the transmission spectrum shown in Fig. 5(a).

An interference dip (denoted as Dip A) and the resonance coupling dip (denoted as Dip B) were selected to measure the performance of the sensor. The responses of the sensor to salinity at the temperature of 25 °C are shown in Fig. 6, where the salinity range is from 0 to 80 ‰ with a step of 10 ‰. The wavelength of the interference dip was seen to be linearly red-shifted, with the increase of the salinity, while the coupling resonance dip wavelength also shifts to the long wavelength region. The coupling resonance will weaken, since the coupling efficiency between the center core and the suspended core decreases with the increase of the external RI. The sensitivities to salinity of Dip A and Dip B were 135.7 pm/‰ and 190.7 pm/‰, respectively. In addition, the temperature responses were also measured for different salinities, and the result are shown in Fig. 7. The sensor was placed in a temperature and humidity chamber, and the temperature was increased from 0 to 35 °C with a step of 5 °C. When the salinity of the NaCl solution is 80 ‰, the temperature sensitivities of Dip A and Dip B were -74.8 pm/°C and -188.2 pm/°C, respectively. The measured results verify the temperature sensitivities are almost identical for different salinities.

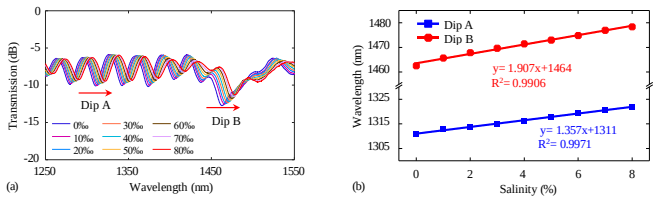

Fig. 6 (a) Transmission spectra of the sensor for different values of salinity. (b) The wavelengths of Dip A and the Dip B as a function of salinity.

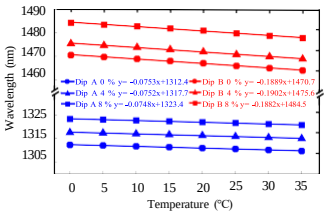

Fig. 7 (a) The wavelengths of Dip A and Dip B as a function of temperature for different salinities.

Based on the above measurement, a sensitivity matrix could be established as follows:

$$\begin{pmatrix} \Delta\lambda_A \\ \Delta\lambda_B \end{pmatrix} = \begin{pmatrix} 135.7\ \text{pm/‰} & -74.8\ \text{pm/°C} \\ 190.7\ \text{pm/‰} & -188.2\ \text{pm/°C} \end{pmatrix} \times \begin{pmatrix} \Delta S \\ \Delta T \end{pmatrix} \quad (5)$$

The sensor based on HATCF was used to detect the characteristics of the RI and the temperature. Before the sensor was submerged into deionized water, there is only one resonance dip at the wavelength of ~1540 nm because the phase-matching wavelengths between center core and two suspended cores are the same. After the sensor was submerged into the deionized water, the initial resonance dip

splits into two resonance dips due to the red-shift of the phase-matching wavelength between the center core and the suspended core 1. The two resonance dips are denoted as dip 1 and dip 2, respectively. Dip 2 is generated by the coupling between center core and suspended core 2 with closed air hole 2, and dip 1 is generated by the coupling between center core and suspended core 1, as shown in Fig. 8 (a).

In the temperature of 25 °C, 35 °C, 45 °C, the RI response of the sensor was measured in glycerinum solutions with the RI range from 1.333 to 1.388 with a step of 0.005. During the measuring process, the sample slot was placed in a temperature chamber to ensure a constant temperature. The transmission spectra for different RIs are shown in Fig. 8 (b). As the RI increases, the resonance dip 1 has a redshift. There is a good linear relationship between the wavelength of dip 1 and the RI. The sensitivity reaches 1369 nm/RIU in the RI range of 1.333-1.388 in 25 °C, as shown in Fig. 8 (c). With the increase of RI around suspended core 1, the effective RI of the fundamental mode in suspended core 1 increases, while that in center core is not changed. Therefore, the phase-matching wavelength between center core and suspended core 1 shows a red-shift. In contrast, the suspended core 2 is isolated from the external environment. The wavelength of resonance dip 2 hardly changes and just fluctuates in the range of 0.05 nm, as shown in Fig. 8 (d), which can be attributed to the temperature fluctuations in the temperature chamber.

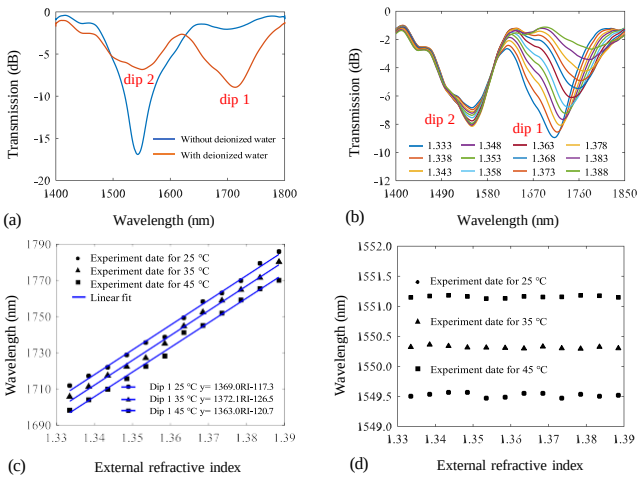

Fig. 8 (a) The transmission spectra of the sensor before and after being submerged into deionized water. (b) The transmission spectrum evolution for different RIs. The RI sensitivities of (c) dip 1 and (d) dip 2 in different temperature.

The temperature characteristics of the sensor were also measured. The sensor was placed in a water bath with deionized water, and the deionized water was heated from 25 to 70 °C and then cooled to 25 °C with a step of 5 °C. With the increase of temperature, the resonance dip 1 has a redshift and the sensitivity is 83.48 pm/°C, while the resonance dip 2 shows a blueshifts with a sensitivity of -500.7 pm/°C.

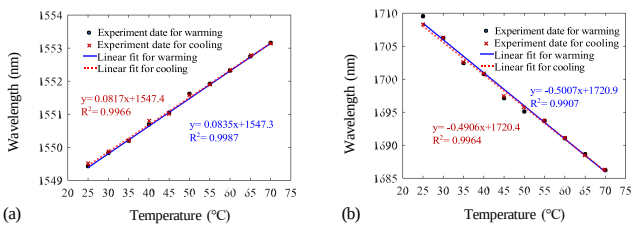

Fig. 9 The temperature responses of (b) dip 1 and (c) dip 2.

Based on the above measurement, a sensitivity matrix could be established as follows:

$$\begin{bmatrix} \Delta\lambda_1 \\ \Delta\lambda_2 \end{bmatrix} = \begin{bmatrix} 1369\text{nm/RIU} & -500.7\text{pm}/^\circ\text{C} \\ 0 & 83.48\text{pm}/^\circ\text{C} \end{bmatrix} \begin{bmatrix} \Delta n \\ \Delta T \end{bmatrix} \quad (7)$$

3. CONCLUSIONS

In conclusion, we have introduced two dual-parameter optical fiber sensors based on HADCF and HATCF respectively. The measured salinity and temperature sensitivities are 190.7 pm/‰ and -188.2 pm/°C for the sensor based on HADCF. The measured RI and temperature sensitivities are 1369 nm/RIU in the range of 1.333-1.388 and 83.48 pm/°C in the range of 25-70 °C for the sensor based on HATCF. Because of good performance, simple structure and high level of integration, the proposed sensors have great application potential in the field of biological detection.

FUNDING STATEMENT

This work was supported by the National Natural Science Foundation of China (62105077, 62175049, 62275061); Natural Science Foundation of Heilongjiang Province in China (YQ2021F002). Fundamental Research Funds for the Central Universities (3072022TS2501, 3072022CF2505).

REFERENCES

[1] P. R. Cooper, **Refractive-index measurements of liquids used in conjunction with optical fibers**, Appl. Opt. vol 22, 1983, pp. 3070-3074.

[2] Q. Wang, L. Kong, Y. Dang, F. Xia, Y. Zhang, Y. Zhao, H. Hu, and J. Li, **High sensitivity refractive index sensor based on splicing points tapered SMF-PCF-SMF structure Mach-Zehnder mode interferometer**, Sens. Actuators B: Chem. vol 225, 2016, pp. 213-220.

[3] C. Teng, P. Shao, R. Min, H. Deng, M. Chen, S. Deng, X. Hu, C. Marques, and L. Yuan, **Simultaneous measurement of refractive index and temperature based on a side-polish and V-groove plastic optical fiber SPR sensor**, Opt. Lett. vol 48, 2023, pp. 235-238.

[4] Q. Wang, W. Wei, M. Guo, and Y. Zhao, **Optimization of cascaded fiber tapered Mach-Zehnder interferometer and refractive index sensing technology**, Sens. Actuators B: Chem. vol 222, 2016, pp. 159-165.

[5] Y. G. Liu, X. Liu, T. Zhang, and W. Zhang, **Integrated FPI-FBG composite all-fiber sensor for simultaneous measurement of liquid refractive index and temperature**, Opt. Laser Technol. vol 111, 2018, pp. 167-171.

[6] M. Q. Chen, T. Y. He, Y. Zhao, and G. Yang, **Ultra-short phase-shifted fiber Bragg grating in a microprobe for refractive index sensor with temperature compensation**, Opt. Laser Technol. vol 157, 2023, pp. 108672-108678.

[7] J. Yang, C. Guan, P. Tian, T. Yuan, Z. Zhu, P. Li, J. Shi, J. Yang, and L. Yuan, **In-fiber refractive index sensor based on single eccentric hole-assisted dual-core fiber**, Opt. Lett. vol 42, 2017, pp. 4470-4473.